Saroj Rout
Mixignal Innovations
Nashua, NH, USA

Sameer Sonkusale
Electrical and Computer Engineering
Tufts University
Medford, MA, USA

ISBN 978-3-319-52218-0 ISBN 978-3-319-52219-7 (eBook)
DOI 10.1007/978-3-319-52219-7

Library of Congress Control Number: 2017930655

Printed on acid-free paper

This Springer imprint is published by Springer Nature
The registered company is Springer International Publishing AG
The registered company address is: Gewerbestrasse 11, 6330 Cham, Switzerland

To our parents

Preface

Metamaterials, first known as left-handed materials (LHMs) or negative-index materials (NIMs), are artificially constructed *effective materials* using periodic structures that are a fraction of the wavelength of the incident electromagnetic wave, resulting in effective electric and magnetic properties (permittivity and permeability) that are unavailable in natural materials. The ability to design effective materials with deterministic electromagnetic properties makes them very attractive for terahertz applications since natural materials do not respond well to this frequency regime.

Since the discovery and experimental demonstration of artificial material with negative permittivity and negative permeability by Sir Pendry et al. in 1996 and 1999, the research interest in metamaterials has significantly increased. In spite of the intense research activities in the last two decades, application of metamaterials to terahertz frequencies is a recent phenomenon. And, terahertz metamaterials embedded with active devices are even a smaller portion of this research landscape. Moreover, the transition from research to real-world application of terahertz metamaterials is still years behind because of numerous implementation challenges.

This book intends to close that gap by providing theoretical background and experimental and fabrication methods in one comprehensive text. This is well suited for engineers and physicists to be able to design, fabricate, and characterize terahertz metamaterial devices in commercial planar semiconductor processes.

Three case studies are covered in detail involving terahertz modulator and detector implemented in commercial gallium arsenide (GaAs) and complementary metal-oxide semiconductor (CMOS) process for imaging and communication applications.

The first three chapters provide the introduction, background theory, and experimental methods which give the reader the motivation and basic background to understand terahertz metamaterials. The last three chapters provide the three case studies of active metamaterials fabricated in planar semiconductor process for terahertz imaging and communication applications.

Chapter 1 begins by providing the motivation for working in the terahertz frequency regime for its numerous important applications and showing, with

quantitative reasoning, why metamaterials are a suitable technology for that regime. An overview of technologies for terahertz wave modulators is presented, which is the primary structure underlying all of the designs in this text.

Chapter 2 reviews some of the basic electromagnetic principles for a basic understanding of metamaterials. One of the key contributions of this text is the analysis of terahertz wave modulators using the Drude–Lorentz model.

Chapter 3 covers the experimental methods for modeling, simulating, and characterizing terahertz metamaterials. A section on CMOS fabrication is introduced with few metamaterial case studies for readers to get familiar with a very accessible process that can be used for limited terahertz metamaterial applications. For metamaterial characterization, terahertz time-domain spectroscopy (THz-TDS) and continuous-wave terahertz spectroscopy (cw-THz) are covered in detail. A section is also dedicated to the alignment of off-axis parabolic mirrors, which is found in most terahertz test setups and should be a valuable resource for anyone doing experiments in this field.

Chapter 4 covers a case study of metamaterial-based terahertz modulator using embedded HEMT devices which is one of the main contributions to the scientific literature by the authors. Design principle of HEMT-controlled metamaterial is covered in detail based on the modulator principle introduced in Chap. 2. Design, fabrication, experimental setup, and test results are also covered in this chapter.

Chapter 5 covers another case study of an all solid-state metamaterial-based terahertz spatial light modulator (SLM) using the HEMT-based modulator described in Chap. 4. The principle behind single-pixel imaging is presented in this chapter followed by design, fabrication, and test of the SLM.

Chapter 6 presents the last case study of a terahertz focal plane array (FPA) using metamaterials in a 0.18 μm CMOS process. The principle of resistive self-fixing detection is covered followed by the design and simulation of the FPA.

Nashua, NH, USA Saroj Rout
Medford, MA, USA Sameer Sonkusale

Acknowledgments

There have been quite a few who have inspired and motivated this work and helped us design, simulate, and characterize. We want to begin by thanking Dr. Willie Padilla whose department colloquiums at Tufts University were to sow the seeds for the contributions we made in this text. We want to thank him for introducing us to this exciting field of metamaterials. We also want to thank his doctoral students Dr. David Shrekenhamer and Chris Bingham for help with the design and simulation of the modulators. David in particular spent countless hours helping us simulate and test the HEMT-based metamaterial modulator we developed. We also want to thank Dr. Richard Averitt and Dr. Andrew Strikwerda for helping us with their terahertz time-domain spectroscopy (THz-TDS) setup for characterizing the modulator.

We thank Dr. Wangren Xu for contributing Sect. 3.2 on design for fabrication in foundry process. Our thanks to Jessie Tovera for assembly of the spatial light modulator (SLM).

Our special thanks to Mr. Charles B. Glaser, editorial director at Springer USA, for encouraging us with writing the proposal of this book and providing us feedback and clarification throughout the writing process.

We acknowledge the support of the Office of Naval Research under US Navy Contracts N00014-07-1-0819 and N00014-09-1-1075, and the National Science Foundation Awards No. ECCS-1002340 and ECCS-1002152.

We also acknowledge the support of DoD Defense University Research Infrastructure Program (DURIP) under grant N00014-12-1-0888 equipment purchase used for test and characterization.

Finally, we want to thank our families for their unconditional love and support without which nothing would ever be possible.

Contents

Chapter 1
Introduction

The primary purpose of this text is to provide analytic and experimental methods to design planar metamaterial based wave modulators for terahertz frequencies, especially for communication and imaging applications. This chapter provides the motivation for the reader by answering two basic questions: why terahertz frequencies and why design metamaterials for that frequency regime.

Section 1.1 introduces the fact behind the so-called terahertz gap and illustrates numerous important examples to show why this frequency regime is interesting. A brief history of various terahertz technologies is provided for the reader to get a historical perspective as well as the state of the art. Section 1.2 introduces the basic concept of metamaterials with a brief history and overview of the topic. A quantitative reason is provided in Sect. 1.2.3 as to why metamaterials are suitable for terahertz frequencies. Section 1.3 provides an overview of technologies for terahertz wave modulators, which is the primary focus of this text.

1.1 Towards Closing the "Terahertz Gap"

The terahertz (THz) regime of the electromagnetic (EM) spectrum is broadly recognized by the frequency range of 100 GHz to 10 THz[1] (where 1 THz corresponds to a frequency of 10^{12} Hz, a wavelength of 300 μm, and photon energy of 4.1 meV) [2, 3]. This region, alternatively called the far-IR, lies between infrared light and the microwave frequencies as shown in Fig. 1.1a.

Most modern devices are based on the response of the electrons in materials to applied EM field and the nature of the response is dependent on the frequency of the EM field. At frequencies few hundred gigahertz and lower, the motion of free electrons forms the basis of most EM devices characterized broadly as *electronics*.

[1] Some define THz to be the submillimeter-wave energy that fills the wavelength range between 1 and 0.1 mm (300 GHz–3 THz) [1].

S. Rout, S. Sonkusale, *Active Metamaterials*, DOI 10.1007/978-3-319-52219-7_1

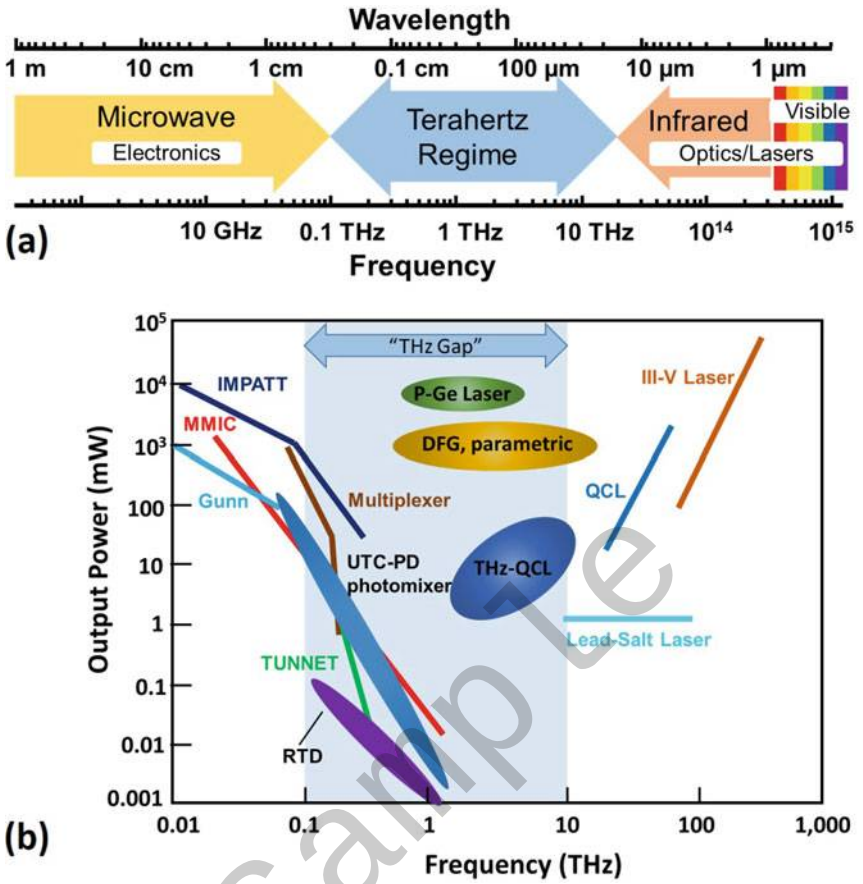

Fig. 1.1 The THz gap—(**a**) THz regime of the EM spectrum extends from 100 GHz to 10 THz, which lies below visible and infrared (IR) wavelengths and above microwave wavelengths. (**b**) Illustration of the THz gap—THz emission power as a function of frequency [4]. *Solid lines* are conventional sources and *oval shapes* denote recent THz sources. IMPATT stands for impact ionization avalanche transit-time diode, MMIC stands for microwave monolithic integrated circuit, TUNNET stands for tunnel injection transit time, multiplexer is a Schottky barrier diode (SBD) frequency multiplier, UTC-PD stands for uni-traveling-carrier photodiode, DFG stands for difference frequency generator and QCL stands for quantum cascade laser

It is well known that fundamental sources of power in electronics exhibit decrease in power with increasing frequency. This is a consequence of few main factors such as characteristic transit distance, for example related to length of a channel in a FET; second is the saturation velocity of carriers in the device, typically 10^5 m/s; and the third being the maximum electric field that is sustainable in a device before breakdown. The accumulation of these limits has led to practical electronic RF

sources around 300 GHz with sub-milliwatt power output [5] and much lower power for frequencies near THz, for example, 15 μW at 1.8 THz for a Schottky multiplier chain [6].

On the other hand, at infrared through optical and ultra-violet wavelengths the devices are characterized as *photonics*. It is also well known that photonics sources exhibit decrease in output power with decreasing frequency and the fundamental reason for this is lack of photon energy to meet the band-gap requirements for most photonics sources: for example, the longest wavelength lead salt laser diodes do not extend below 15 THz. Thus, in between these two regions, there exists the so-called THz gap, where the efficiency of electronic and photonics devices tends to taper off as illustrated in Fig. 1.1b. Because of the lack of natural materials that respond to the THz region of EM spectrum, this regime is arguably the least developed and least understood of the EM spectrum [2, 4, 5].

1.1.1 Why Is the "Terahertz Gap" Interesting

The past three decades have seen a revolution in THz systems motivated in part by vast range of unique applications ranging from imaging, sensing to spectroscopy [7], as shown in Fig. 1.2. Astronomy and space research has been one of the early drivers for THz research because of the vast amount of spectral information available concerning the presence of abundant molecules such as oxygen, water, and carbon monoxide in stellar dusts, comets, and planets that have unique THz spectral signatures [8]. The application of THz sources in astronomy is as local oscillator sources for submillimeter-wave heterodyne receivers used to perform high-resolution spectroscopy [1]. Back on Earth, the two most pervasive applications for

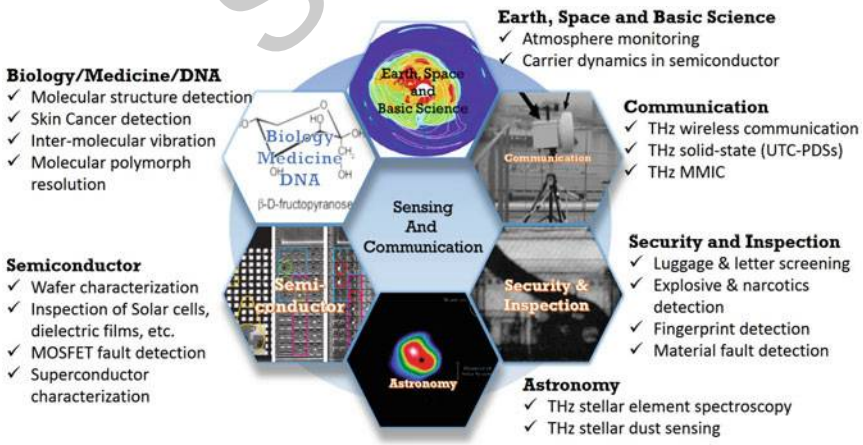

Fig. 1.2 A snapshot of some of the unique applications in the terahertz frequency regime

terahertz technology have been in the areas of plasma fusion diagnostics and gas spectroscopy [9]. THz spectroscopy development has been an active research topic due to its potential in extracting material characteristics that are unavailable when using other frequency bands. Terahertz spectroscopy has been used to determine the carrier concentration and mobility of doped semiconductors such as GaAs and silicon wafers [10, 11] and high-temperature superconductor characterization [12]. THz systems have been developed for biomedical applications that are facilitated by the fact that the collective vibrational modes of many proteins and DNA molecules are predicted to occur in the THz range [13]. A further biomedical application of THz systems is the THz biosensor. A simple biosensor has been demonstrated for detecting the glycoprotein avidin after binding with vitamin H (biotin) using the technique of differential THz-TDS [14].

In recent years, terahertz (THz) imaging has captured significant interest due to its ability to penetrate most dielectric materials and non-polar liquids [15, 16], allowing stand-off spectroscopy for security screening [17] and illicit drug detection [18]. Its harmless interaction with human tissue has resulted in wide range of applications such as bio-detection [19] and skin cancer detection [20], to name a few. Another attraction of THz imaging is largely due to the availability of phase-sensitive spectroscopic images, which holds the potential for material identification or "functional imaging." THz systems are ideal for imaging dry dielectric substances including paper, plastics and ceramics. These materials are relatively non-absorbing in this frequency range, yet different materials may be easily discriminated on the basis of their refractive index, which is extracted from the THz phase information. Many such materials are opaque at optical frequencies, and provide very low contrast for X-rays. THz imaging systems may therefore find important niche applications in security screening and manufacturing quality control [21]. Interest in using THz imaging to study cellular structure is also increasing [22].

Another emerging area for the terahertz regime is high-speed wireless communication. The demand for high-speed wireless access is increasing due to large amounts of data needed for new emerging applications such as the consumer market that is already demanding 20, 40 and 100 Gbit/s wireless technologies for Super Hi-Vision (SHV) and Ultra High-Def (UHD) TV data [23]. Terahertz (THz) carrier frequencies will offer the advantage of higher data speed, sub-millimeter antenna size and short range security especially suitable for portable devices. Although they are susceptible to atmospheric loss, THz digital communication systems have been demonstrated near certain windows, especially around the 300–400 GHz range that has shown promise for high bit-rate data transmission [23–25].

Next we show two examples of terahertz systems to highlight the significance of this frequency regime.

1.1.1.1 Continuous-Wave Terahertz System for Inspection Applications

The unique property of terahertz waves to penetrate most dielectric materials allows for stand-off spectroscopy of dangerous substances making them an ideal candidate for security screening applications. One such system, a compact continuous-wave

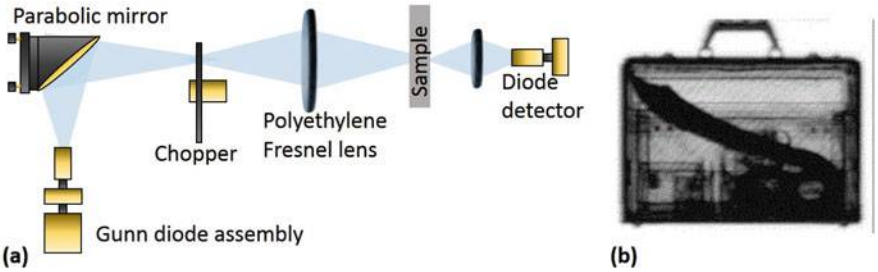

Fig. 1.3 Continuous-wave (cw) terahertz system for inspection applications. (**a**) Schematic diagram of the imaging system in transmission geometry. (**b**) Image of a briefcase holding a large knife and various harmless contents such as a compact disc, a video cassette, and audio cassette and pens [17]

(cw) 0.2 THz imaging system using entirely electronic generation and detection with a minimal number of components is shown in Fig. 1.3a [17]. The system consists of a frequency-doubled Gunn diode oscillator with an output power of 12 mW as a source, and a Schottky diode as the detector. After being emitted by the Gunn diode, the beam is focused by an parabolic mirror to a 4 mm spot where it is modulated by an optical chopper at 1.2 kHz. The chopped beam is focused twice, one on the sample and again on the diode detector by a pair THz optics. The sample is mounted on a translation stage to raster scan the object.

Figure 1.3b shows a 0.2 THz cw scan of a standard size leather briefcase, containing benign and suspicious items. The strengths of the system can be immediately seen: objects can be recognized fairly easily, and since the radiation involved is non-ionizing, it poses little threat to human beings.

1.1.1.2 Giga-Bit Wireless Link Using 300–400 GHz Bands

Because of demand for high-speed wireless access, there is an urgency for designing wireless systems with data speeds of more than 1 Gbit/s. Figure 1.4 shows a block diagram of a 300–400 GHz band system using a photonics-based transmitter and receiver [26]. This system is intended for use in short-distance (∼0.5 m) applications. An optical RF signal is generated by heterodyning the two wavelengths of light from the wavelength-tunable light sources. The optical signal is digitally modulated by a optical intensity modulator driven by a pulse pattern generator (PPG). Finally, the optical signal is converted to an electrical signal by the modified Uni-Traveling-Carrier-Photodiode (UTC-PD). The THz wave is emitted to free space via a horn antenna with a gain of 25 dBi, and it is collimated by a 2-inch-diameter Teflon lens. The receiver consists of a Schottky barrier diode and an IF filter followed by a low-noise pre-amplifier and a limiting amplifier. The envelope detection is performed by the Schottky-Barrier-Diode (SBD) for amplitude shift keying (ASK) modulation. The inset in Fig. 1.4 shows the eye diagram at 14 Gbit/s which is evidently error-free from the clear eye opening.

Chapter 2
Background Theory

This chapter reviews some of the fundamental electromagnetic principles for a basic understanding of metamaterials and metamaterials as terahertz modulator. Section 2.1 covers the basic electromagnetic properties of materials with non-positive dielectric parameters, permitivity (ϵ) and permeability (μ). In Sect. 2.2, basic Lorentz oscillator model for permitivity is developed to illustrate the anomalous dispersion behavior that is fundamental to the modulator design. Finally, the basic principle of wave modulation using metamaterials is formulated in Sect. 2.3.

Complete and rigorous electromagnetic analysis is beyond the scope of this book. For such in-depth analysis there is an excellent collection of standard textbooks such as Landau et al. [1], Jackson [2], Kong [3]. For detailed analysis on optical properties of materials, an excellent reference is Wooten [4]. For further exploration of metamaterials, readers are referred to texts on metamaterials such as Ramakrishna et al. [5], Tretyakov [6], Eleftheriades et al. [7], Caloz et al. [8], Engheta et al. [9], Pendry [10].

2.1 Plane Waves in a Nonconducting Medium

Material response to electromagnetic waves can fundamentally be expressed by the Maxwell equations at the atomic length scales. However, in most cases we are not interested in the fast variation of electric and magnetic fields at those microscopic scales, instead a macroscopic description is sufficiently accurate. At a macroscopic level, the Maxwell equations are written as

$$\nabla \cdot \mathbf{D} = \rho \tag{2.1}$$

$$\nabla \cdot \mathbf{B} = 0 \tag{2.2}$$

$$\nabla \times \mathbf{E} + \frac{\partial \mathbf{B}}{\partial t} = 0 \tag{2.3}$$

S. Rout, S. Sonkusale, *Active Metamaterials*, DOI 10.1007/978-3-319-52219-7_2

$$\nabla \times \mathbf{H} - \frac{\partial \mathbf{D}}{\partial t} = \mathbf{J} \tag{2.4}$$

where **E** and **H** are the macroscopic electric and magnetic fields, **D** is the displacement field and **B** is the magnetic induction. Similarly, **J** and **j** are the macroscopic net charge and current densities. These macroscopic expressions are averaged over lengths that is large compared to inter-molecular distance but still only a fraction of wavelength of the applied fields, resulting in a homogeneous approximation of the material. A detailed derivation of these equations from microscopic Maxwell equations can be found in Jackson [2].

The metamaterials discussed in this text can be macroscopically approximated as dielectrics or nonconductors that are a devoid of free charge, and the Maxwell equations (2.1)–(2.4) can be reduced to

$$\nabla \cdot \mathbf{D} = 0 \tag{2.5}$$

$$\nabla \cdot \mathbf{B} = 0 \tag{2.6}$$

$$\nabla \times \mathbf{E} + \frac{\partial \mathbf{B}}{\partial t} = 0 \tag{2.7}$$

$$\nabla \times \mathbf{H} - \frac{\partial \mathbf{D}}{\partial t} = 0 \tag{2.8}$$

In most materials, which are linear and isotropic, the displacement field **D** is directly proportional to the applied electric field **E**:

$$\mathbf{D} = \epsilon \mathbf{E} \tag{2.9}$$

where ϵ which is dispersive, i.e., function of the frequency ω, $\mathbf{D} = \epsilon(\omega)\mathbf{E}$. The dispersion is associated with the inertia of the dipoles due to the mass of electrons. In addition to being dispersive, ϵ also requires to be a complex function on the account of causality where the imaginary part is attributed to the loss or the absorbed energy in the medium. For a succinct proof of ϵ as a dispersive and complex function, the reader is referred to Ramamkrishna et al. [5].

A similar analysis holds true for the magnetic permeability,

$$\mathbf{B} = \mu \mathbf{H} \tag{2.10}$$

where is μ is dispersive and a complex function as well.

The causality and analyticity domain of $\epsilon(\omega)/\epsilon_0$ allows the use of Cauchy's theorem to relate the real and the imaginary part of $\epsilon(\omega)/\epsilon_0$, known as the Kramers–Kronig relations, and is expressed as (Jackson [2])

$$\mathrm{Re}[\epsilon(\omega)/\epsilon_0] = 1 + \frac{1}{\pi} \mathrm{P} \int_{-\infty}^{\infty} \frac{\mathrm{Im}[\epsilon(\omega')/\epsilon_0]}{\omega' - \omega} d\omega' \tag{2.11}$$

$$\mathrm{Im}[\epsilon(\omega)/\epsilon_0] = -\frac{1}{\pi}\,\mathrm{P}\int_{-\infty}^{\infty}\frac{\mathrm{Re}[\epsilon(\omega')/\epsilon_0]-1}{\omega'-\omega}d\omega' \tag{2.12}$$

where P means the principal value of the Cauchy's integral. This relation is regarded as very fundamental to the dispersion nature of ϵ. This relation allows the calculation of $\mathrm{Re}[\epsilon(\omega)]$ from the experimental data of $\mathrm{Im}[\epsilon(\omega)]$ from absorption experiments.

For sinusoidal solutions ($e^{-i\omega t}$), the equations for the $\mathbf{E}(\omega, \mathbf{x})$,etc.

$$\begin{aligned} \nabla\cdot\mathbf{B} &= 0, \qquad \nabla\times\mathbf{E} - i\omega\mathbf{B} = 0 \\ \nabla\cdot\mathbf{D} &= 0, \qquad \nabla\times\mathbf{H} + i\omega\mathbf{D} = 0 \end{aligned} \tag{2.13}$$

For uniform isotropic linear media, $\mathbf{D} = \epsilon\mathbf{E}, \mathbf{B} = \mu\mathbf{H}$ where ϵ and μ in general maybe complex functions of ω. For real and positive ϵ and μ (no losses), $\mathbf{D}$ and $\mathbf{B}$ can be substituted in Eq. (2.13) to get the Helmholtz wave equation (See Appendix A.1)

$$\left(\nabla^2 + \mu\epsilon\omega^2\right)\left\{\begin{matrix}\mathbf{E}\\ \mathbf{B}\end{matrix}\right\} = 0 \tag{2.14}$$

A plane-wave solution, traveling in the x direction, that satisfies both the Maxwell's equation (2.13) and the Helmholtz's equation (2.14) can be shown to be

$$\begin{aligned} \mathbf{E}(\mathbf{x}, t) &= \mathbf{E}_0 e^{i(kx-\omega t)} \\ \mathbf{B}(\mathbf{x}, t) &= \mathbf{B}_0 e^{i(kx-\omega t)} \end{aligned} \tag{2.15}$$

where k is the wave number

$$k = \sqrt{\epsilon\mu}\,\omega \tag{2.16}$$

The *phase velocity* of the wave is

$$v = \frac{\omega}{k} = \frac{1}{\sqrt{\epsilon\mu}} = \frac{c}{n} \tag{2.17}$$

The quantity n is called the *index of refraction* that can be expressed as

$$n = \sqrt{\frac{\mu}{\mu_0}\frac{\epsilon}{\epsilon_0}} = \sqrt{\mu_r\epsilon_r} \tag{2.18}$$

The wave impedance Z can be expressed as

$$Z = \frac{E_0}{H_0} = \frac{k}{\omega\epsilon} = \frac{1}{v\epsilon} = \sqrt{\frac{\mu}{\epsilon}} = \zeta Z_0 \quad \zeta = \frac{\mu_r}{\epsilon_r} \tag{2.19}$$

2.1.1 Negative Refractive Index

It can be seen from Helmholtz's equation (2.14) that propagating waves exist in materials whether ϵ and μ are both positive or negative. In this equation, ϵ and μ enter as a product, so it would not appear to matter whether both the signs are positive or negative. Conventionally, we always express the refractive index n as $+\sqrt{\mu_r \epsilon_r}$ for positive materials ($\epsilon > 0, \mu > 0$).

But, one needs to be careful in taking the square root for $n = \pm\sqrt{\mu_r \epsilon_r}$, that is resolved by proper analysis. In real materials, the constitutive parameters (ϵ, μ) are complex quantities and causality requires the imaginary part to be positive since the materials are passive. For a left-handed material (LHM), the constitutive parameters satisfy

$$\begin{aligned} \epsilon_r &= e^{i\phi_\epsilon}, \quad \phi_\epsilon \in (\pi/2, \pi] \\ \mu_r &= e^{i\phi_\mu}, \quad \phi_\mu \in (\pi/2, \pi] \end{aligned} \tag{2.20}$$

and now the refractive index can be expressed as

$$n = \sqrt{\epsilon_r \mu_r} = e^{i\phi_\epsilon/2} e^{i\phi_\mu/2} \tag{2.21}$$

and causality requires the imaginary part of the each $\sqrt{\epsilon}$ and $\sqrt{\mu}$ be positive

$$n = (\epsilon_r' + i\epsilon_r'')(\mu_r' + i\mu_r'') \tag{2.22}$$

where $\epsilon_r' = \cos(\phi_\epsilon/2)$, $\epsilon_r'' = \sin(\phi_\epsilon/2)$, $\mu_r' = \cos(\phi_\mu/2)$ and $\mu_r'' = \sin(\phi_\mu/2)$.

If the real part of each of the complex quantity in Eq. (2.22) goes to zero, the positive imaginary values result in a real $n < 0$. Therefore,

$$n = -\sqrt{\epsilon_r \mu_r}, \quad \epsilon_r < 0, \mu_r < 0 \tag{2.23}$$

A detailed derivation of it can be found in [11, 12].

2.1.2 Propagation of Waves in Left-Handed Material

For plane monochromatic wave proportional to $\exp(ikx - i\omega t)$, Eqs. (2.1)–(2.4) along with $\mathbf{D} = \epsilon\mathbf{E}, \mathbf{B} = \mu\mathbf{H}$ reduce to [13] (See Appendix A.2)

$$\begin{aligned} \mathbf{k} \times \mathbf{E} &= \omega\mu\mathbf{H} \\ \mathbf{k} \times \mathbf{H} &= -\omega\epsilon\mathbf{E} \end{aligned} \tag{2.24}$$

It can be seen from these equations that for materials with $\epsilon > 0$ and $\mu > 0$ they form a right-handed triplet vectors and so the term *Right-Handed Materials* (RHM), and for materials with $\epsilon < 0$ and $\mu < 0$ they form a left-handed triplet vectors and so the term *Left-Handed Materials* (LHM).

This should not be confused with the left-handed chiral optical materials which are completely different. This has prompted authors to call these *backward wave media* [14], *negative phase velocity media* [12], *double negative media* [11] or *negative refractive index materials* [15].

The energy flux carried by the wave is determined by the Poynting vector **S**, given by

$$\mathbf{S} = \mathbf{E} \times \mathbf{H} \tag{2.25}$$

and the direction of the vector is given by the right-hand rule which is the same for right-handed materials. Since Poynting's Theorem is derived by considering conservation of energy [2], we can think of a matched interface of a right-handed material with a left-handed material and the energy flow has to be in the same direction. Therefore, according to Eq. (2.25) the vector **S** is in parallel with the wave vector **k** for right-handed materials and is anti-parallel for left-handed materials.

2.1.3 Propagation of Waves in Single Negative Medium

A single negative medium has either $\epsilon < 0$ or $\mu < 0$. For this analysis, we will assume $\epsilon < 0$ and $\mu = \mu_0$. The wave number k can be expressed as

$$k = \omega\sqrt{\mu_0|\epsilon_r|}e^{i\phi_e/2} = k' + ik'' \tag{2.26}$$

By substituting k (2.26) in a plane wave ($\mathbf{E}(x,t) = \mathbf{E}_0 e^{i(kx-\omega t)}$), it can be expanded to

$$\mathbf{E}(x,t) = e^{-k''x}\mathbf{E}_0 e^{i(k'x-\omega t)} \tag{2.27}$$

The analysis for $\mu < 0, \epsilon > 0$ is similar. Therefore, the propagating wave in a single negative media is a decaying wave front.

2.2 Dispersion in Nonconductors

In the previous section, it has been shown that the propagation of EM waves in nonconducting media is governed by two properties of the material, which was assumed to be constant: the permittivity ϵ, and the permeability μ. It is well known from optics that the *refractive index* ($n = c\sqrt{\epsilon\mu}$) is a function of ω. Thus a prism bends blue light more sharply than red, spreading white light into a rainbow of colors. This phenomena is called *dispersion* and whenever the speed of a wave varies

with frequency, the supportive medium is called *dispersive*. Although both ϵ and μ are function of ω, in practice, μ is very close to μ_0, for most natural materials, and its variation with ω is insignificant [16].

2.2.1 Lorentz Oscillator Model for Permitivity

The classical theory of the absorption and dispersion for nonconductors (insulators) is due mainly to Lorentz. The Drude model is applicable to free-electron metals. Although these models were based on classical ad hoc formulation, the quantum mechanical analogs are strikingly similar and to date, the Drude–Lorentz models are still very useful for developing a feel for optical properties of solids.

The Lorentz model considers an atom with electrons bound to the nucleus using a model described by a small mass tied to a large mass by spring. The motion of an electron is then described by

$$m\left[\ddot{\mathbf{x}} + \gamma\dot{\mathbf{x}} + \omega_0^2\mathbf{x}\right] = -e\mathbf{E}(\mathbf{x}, t) \tag{2.28}$$

where $m\gamma\dot{\mathbf{x}}$ is the damping force representing the energy loss mechanism which arises due to radiation from an atom due to different scattering mechanisms. The term $m\omega_0^2\mathbf{x}$ is the Hooke's law restoring force in the *electron oscillator* model. In the context of a classical model, there are two main assumptions in Eq. (2.28). The nucleus has been assumed to have infinite mass and the small magnetic force $-e\mathbf{v}\times\mathbf{B}/c$ on the electron due to the magnetic component has been neglected.

For a sinusoid electric field with frequency ω as $e^{-i\omega t}$, the displacement vector $\mathbf{x}$ is the solution of Eq. (2.28) and the dipole moment $\mathbf{p}$ contributed by each electron is [2]

$$\mathbf{p} = -e\mathbf{x} = \left[\left(\frac{e^2}{m_e}\right)\frac{1}{(\omega_0^2 - \omega^2) - i\omega\gamma}\right]\mathbf{E} = \xi(\omega)\mathbf{E} \tag{2.29}$$

where $\xi(\omega)$ is the frequency dependent atomic polarizability. Assuming a linear relationship between $\mathbf{p}$ and $\mathbf{E}$ due to small displacements, $\xi(\omega)$ is a complex quantity because of the damping term in the oscillator model.

For N atoms per unit volume, the macroscopic polarization is [4]

$$\mathbf{P} = N\langle\mathbf{p}\rangle = N\xi(\omega)\langle\mathbf{E}\rangle = \epsilon_0\chi(\omega)\mathbf{E} \tag{2.30}$$

where $\chi(\omega) = N\xi(\omega)/\epsilon_0$ is the frequency dependent complex susceptibility that is defined in relation to the constitutive parameters as

$$\mathbf{D} = \epsilon_0(1 + \chi(\omega))\mathbf{E} = \epsilon_0\epsilon_r(\omega)\mathbf{E} \tag{2.31}$$

Using Eqs. (2.29)–(2.31), the relative permitivity $\epsilon_r(\omega)$ is

$$\epsilon_r(\omega) = 1 + \frac{\omega_p^2}{(\omega_0^2 - \omega^2) - i\omega\gamma}, \qquad \omega_p^2 = \frac{Ne^2}{m_e\epsilon_0} \tag{2.32}$$

where ω_p is the plasma frequency of the insulator which is the oscillating frequency in Drude model where the restoring force term $m_e\omega\gamma$ is zero. In other words, the Drude model for metals is obtained directly from the Lorentz model for insulators simply by equating the restoring force to zero.

2.2.2 *Anomalous Dispersion and Resonant Absorption*

From the complex permitivity expression in Eq. (2.32), the real and imaginary part of $\epsilon_r = \epsilon_r' + i\epsilon_r''$ can be written as

$$\begin{aligned} \epsilon_r'(\omega) &= 1 + \omega_p^2 \frac{\omega_0^2 - \omega^2}{(\omega_0^2 - \omega^2)^2 + \omega^2\gamma^2} \\ \epsilon_r''(\omega) &= \omega_p^2 \frac{\omega\gamma}{(\omega_0^2 - \omega^2)^2 + \omega^2\gamma^2} \end{aligned} \tag{2.33}$$

where $\epsilon_r' = \mathtt{Re}[\epsilon_r]$ and $\epsilon_r'' = \mathtt{Im}[\epsilon_r]$. The imaginary part is directly associated with the absorption of the incident wave and also when the real part is negative. The frequency dependence of ϵ_r' and ϵ_r'' is plotted in Fig. 2.1. Except for a narrow region around the resonance, ϵ_r' increases with frequency called the normal dispersion. In the narrow region of the resonance it decreases with frequency called *anomalous dispersion*. This region is also the frequency interval of maximum absorption as will be shown later in this section. The width of this region is equal to the loss factor γ.

With ϵ now a complex function of ω, the dispersive medium admits x-polarized plane-wave solutions, as before,

$$\mathbf{E}(x, t) = \mathbf{E}_0 e^{i(kx - \omega t)} \tag{2.34}$$

However, the wave number $k = \omega\sqrt{\epsilon\mu}$ is complex, because ϵ is complex. Writing k in terms of real and imaginary parts of the refractive index

$$k = \beta + i\frac{\alpha}{2} \tag{2.35}$$

equation (2.34) becomes

$$\mathbf{E}(x, t) = \mathbf{E}_0 e^{-\alpha x/2} e^{i(\beta x - \omega t)} \tag{2.36}$$

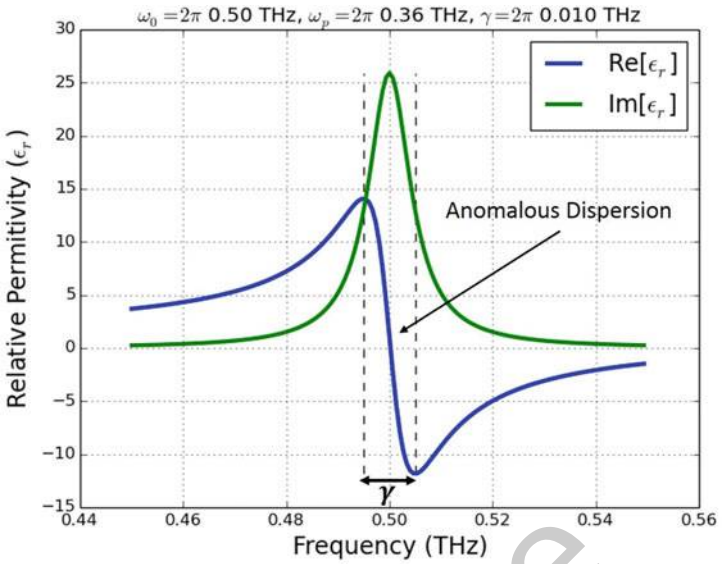

Fig. 2.1 Real and imaginary parts of the dielectric constant $\epsilon(\omega)/\epsilon_0$ in the neighborhood of a resonance. The region of anomalous dispersion is also the frequency interval for the maximum absorption

Evidently, $\alpha/2$ measures the *attenuation* of the wave. Because the *intensity* is proportional to E^2, it falls off as $e^{-\alpha x}$, α is called the *absorption coefficient*. For non-magnetic material ($\mu = \mu_0$), the complex frequency dependent refractive index n can be expressed as

$$n = n_R + in_I = \sqrt{\epsilon_r' + i\epsilon_r''} \tag{2.37}$$

where the n_R and n_I are the real and imaginary part of complex n known as the *ordinary refractive index* and *extinction coefficient*, respectively.

Squaring and equating both sides of Eq. (2.37) we get

$$\epsilon_r' = n_R^2 - n_I^2, \qquad \epsilon_r'' = 2n_R n_I \tag{2.38}$$

From Eq. (2.38), the real and imaginary part of the refractive index are

$$n_R = \left\{ \frac{1}{2} \left[\sqrt{(\epsilon_r')^2 + (\epsilon_r'')^2} + \epsilon_r' \right] \right\}^{1/2}$$
$$n_I = \left\{ \frac{1}{2} \left[\sqrt{(\epsilon_r')^2 + (\epsilon_r'')^2} - \epsilon_r' \right] \right\}^{1/2} \tag{2.39}$$

Now, the absorption coefficient α can be expressed in terms of the refractive index using the relation

$$k = n\omega\sqrt{\epsilon_0\mu_0} = k_0\omega(n_R + in_I), \qquad k_0 = \sqrt{\epsilon_0\mu_0} \tag{2.40}$$

From Eq. (2.40) we can express the absorption coefficient as

$$\alpha = 2k_0\omega n_I \tag{2.41}$$

Typically, for analyzing absorption around the resonance, n_I is sufficient indicator since ω does not change appreciably in that region.

Another optical parameter that provides independent information about the material in the frequency of interest is the reflection coefficient. From Eq. (2.39), the reflection coefficient at normal incidence is given by Wooten [4]

$$R = \frac{(n_R - 1)^2 + n_I^2}{(n_R + 1)^2 + n_I^2} \tag{2.42}$$

The plots for the real/imaginary part of the refractive index [Eq. (2.39)] and the reflection coefficient [Eq. (2.42)] are shown in Fig. 2.2. From the plots, we can see the implications of the frequency dependence of ϵ_r' and ϵ_r''. The plots show four distinct regions, transmission, absorption, reflection, and transmission again.

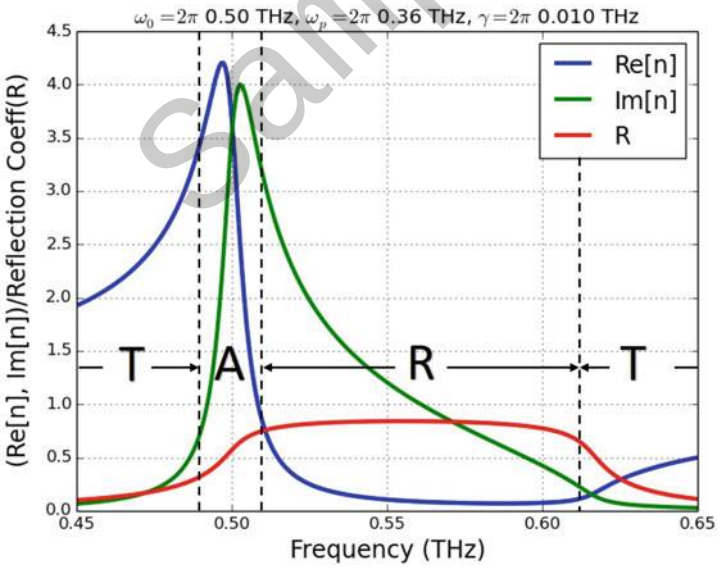

Fig. 2.2 Plots of the real and imaginary part of the refractive index [Eq. (2.39)] and the reflection coefficient [Eq. (2.42)] for an example material with $\omega_0 = 2\pi 0.5$ THz, $\omega_p = 2\pi 0.36$ THz and $\gamma = 2\pi 0.01$ THz

Before the onset of the resonance, the material behaves as a positive refractive index transmissive material. Then, for roughly the band around resonance ($\omega_0 \pm \gamma/2$), the material behaves as an absorber, reflective after that and for frequencies much higher than the plasma frequency, its transmissive again.

These plots give an insight on the considerations for building a metamaterial based modulator. By dynamically controlling the absorption peak, one can modulate an EM wave passing through the metamaterial around the resonance frequency.

2.3 Metamaterial as a Modulator

As explained in Sect. 1.2.2.2, the electrically coupled LC resonator (ELC) based metamaterial is suitable for planar design since the incident field can be incident to the normal of the device plane. For the ELC resonator shown in Fig. 2.3a, the average permittivity, ignoring the spatial dispersion, is of the Lorentz-like form [17–19]

$$\epsilon_{ELC} = \epsilon_a \left[1 - \frac{Ff^2}{f^2 - f_0^2 + i\gamma f} \right] \tag{2.43}$$

where ϵ_a is the permittivity of the background material, e.g. FR4, GaAs substrate, etc., $f_0 = 1/\sqrt{LC}$ is the resonant frequency in terms of its equivalent circuit parameters (Fig. 2.3b), γ is associated with the loss (R_{loss} in Fig. 2.3b), and F is associated with filing factor of the geometry of the unit cell. The real and imaginary part of the permittivity from Eq. (2.43) is plotted in Fig. 2.3c for an example design with $f_0 = 0.5\,\text{THz}$, $\gamma = 0.01\,\text{THz}$, and $F = 0.5$. The response is similar to the Lorentz oscillator model of non-conductors derived in Eq. (2.32). As observed in Fig. 2.2, the absorption of non-conducting materials is maximum in the vicinity

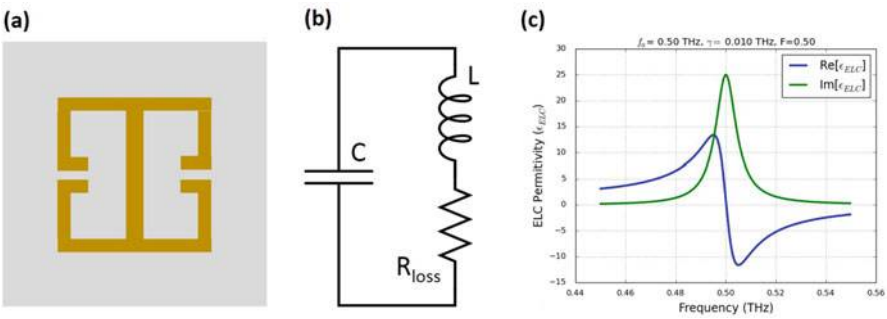

Fig. 2.3 (**a**) An ELC element used in most electric metamaterial design. (**b**) An equivalent circuit of the MM unit cell (**c**) Average permittivity (real and imaginary) of the MM [Eq. (2.43)] for an example design with $f_0 = 0.5\,\text{THz}$, $\gamma = 0.01\,\text{THz}$, and $F = 0.5$

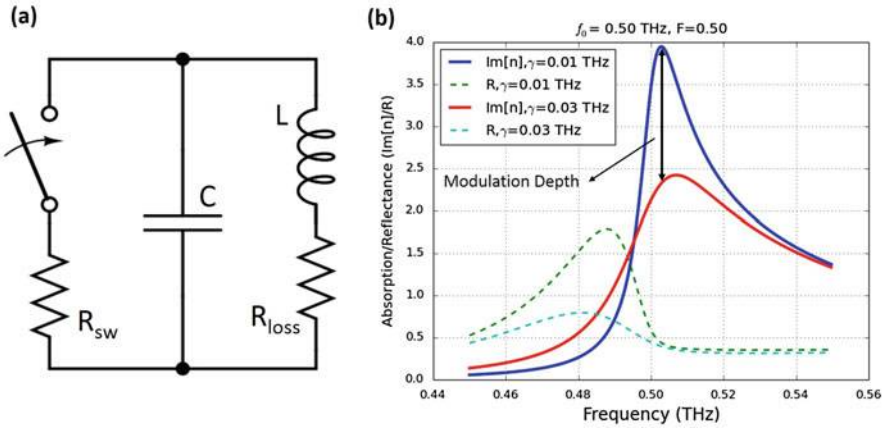

Fig. 2.4 (**a**) A conceptual circuit equivalent of a metamaterial based modulator (**b**) Absorption and reflectance plot of an ELC based metamaterial with and without the modulation resistance (R_{sw})

of molecular resonance frequency. It follows from that observation that, in order to design a metamaterial based modulator for a desired frequency, the resonance frequency of the metamaterial should be designed for that desired frequency and a dynamic method should be devised to either shift the resonance frequency or weaken the resonance by adding loss to the resonator.

One such method is shown conceptually in Fig. 2.4a where a resistive element is used to shunt the MM capacitance of the split gap to weaken the resonance. Assuming the shunt resistor changes the dissipation factor γ from 0.01 to 0.05 THz, the imaginary part of the complex refractive index [n in Eq. (2.39)], which corresponds to the absorption coefficient, is plotted in Fig. 2.4b. It can be seen from the plot that the absorption around the resonance frequency ($f_0 = 0.5$ THz) drops by approximately 40%. The reflectance plot shows little change around the modulation frequency. Terahertz modulators have been demonstrated based on this principle of shunting the split gap capacitance by optically pumping the substrate [20, 21] or electrically injecting carriers [22], a schematic of the basic structure shown in Fig. 1.10. This is the fundamental principle behind the metamaterial based terahertz modulator design in this work that is covered in depth in Chap. 4.

Metamaterial based terahertz modulators have also been demonstrated by dynamically controlling the capacitance or the inductance of the split gap capacitance. A dynamic terahertz metamaterial was realized by dynamically controlling the capacitance of the split gap by optically pumping the substrate and experimentally demonstrated by Chen et al. [23], a schematic of the structure shown in Fig. 1.9. The same work [23] also computationally demonstrated a dynamic terahertz metamaterial by controlling the inductance of the metamaterial unit cell as shown in Fig. 2.5.

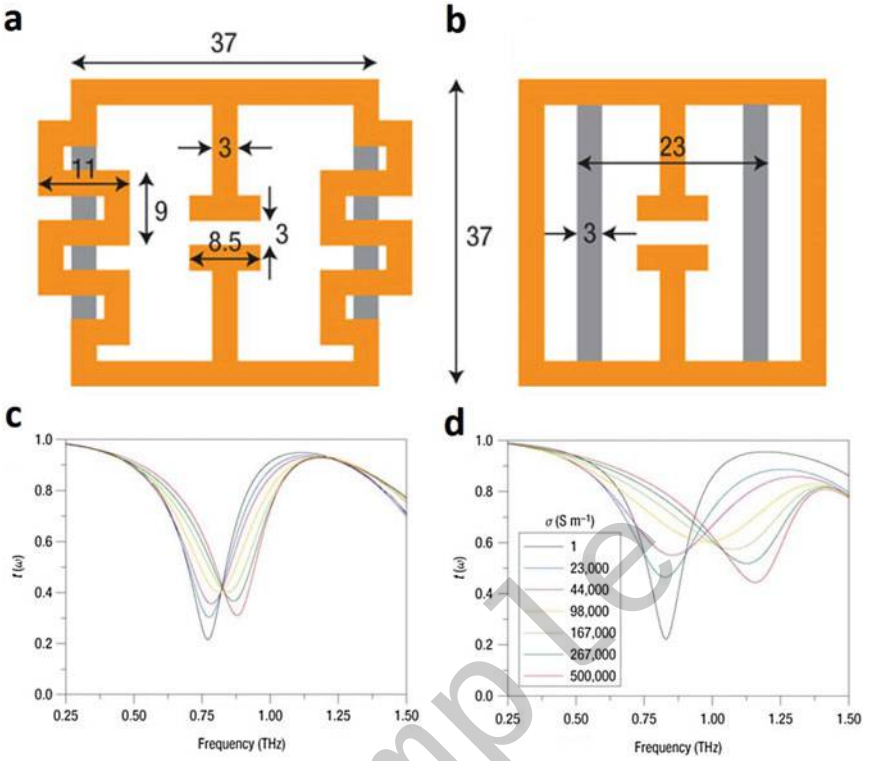

Fig. 2.5 An inductance tune dynamic terahertz metamaterial [23]. (**a**), (**b**) The photoexcited silicon regions form parallel current paths through the meandering loop sections (**a**) and across the regular loop sections (**b**) to effectively modify the inductance of the SRRs. The metal and silicon regions are displayed in *orange* and *grey*, respectively. The dimensions are shown in micrometers. (**c**), (**d**) Simulations of the structure of (**a**) and the structure of (**b**), both using the silicon conductivity values shown in the key

References

1. L.D. Landau, J.S. Bell, M.J. Kearsley, L.P. Pitaevskii, E.M. Lifshitz, J.B. Sykes, *Electrodynamics of Continuous Media* (Elsevier, Amsterdam, 1984)
2. J.D. Jackson, *Classical Electrodynamics*, 3rd edn. (Wiley, New York, 1998)
3. J.A. Kong, *Electromagnetic Wave Theory* (Wiley, New York, 1990)
4. F. Wooten, *Optical Properties of Solids* (Academic, New York, 2013)
5. S.A. Ramakrishna, T.M. Grzegorczyk, *Physics and Applications of Negative Refractive Index Materials* (CRC Press, Boca Raton, 2008)
6. S. Tretyakov, *Analytical Modeling in Applied Electromagnetics* (Artech House, Norwood, 2003)
7. G.V. Eleftheriades, K.G. Balmain, *Negative-Refraction Metamaterials: Fundamental Principles and Applications* (Wiley, New York, 2005)
8. C. Caloz, T. Itoh, *Electromagnetic Metamaterials: Transmission Line Theory and Microwave Applications: The Engineering Approach* (Wiley, New York, 2006)

9. N. Engheta, R.W. Ziolkowski, *Metamaterials: Physics and Engineering Explorations* (Wiley, New York, 2006)
10. J. Pendry, *Fundamentals and Applications of Negative Refraction in Metama* (Princeton University Press, Princeton, 2008)
11. R.W. Ziolkowski, E. Heyman, Phys. Rev. E **64**(5), 056625 (2001)
12. M.W. McCall, A. Lakhtakia, W.S. Weiglhofer, Eur. J. Phys. **23**(3), 353 (2002)
13. V. Veselago, Soviet Phys. Uspekh **10**(4), 509 (1968)
14. I.V. Lindell, S.A. Tretyakov, K.I. Nikoskinen, S. Ilvonen, Microwave Opt. Tech. Lett. **31**(2), 129 (2001)
15. W.J. Padilla, D.N. Basov, D.R. Smith, Mat. Today **9**(7–8), 28 (2006)
16. D.J. Griffiths, *Introduction to Electrodynamics* (Pearson, Boston, 2013)
17. R. Liu, T.J. Cui, D. Huang, B. Zhao, D.R. Smith, Phys. Rev. E **76**(2), 026606 (2007)
18. D.R. Smith, Phys. Rev. E **81**(3), 036605 (2010)
19. B.J. Arritt, D.R. Smith, T. Khraishi, J. Appl. Phys. **109**(7), 073512 (2011)
20. W.J. Padilla, A.J. Taylor, C. Highstrete, M. Lee, R.D. Averitt, Phys. Rev. Lett. **96**(10), 107401 (2006)
21. H.T. Chen, W.J. Padilla, J.M.O. Zide, S.R. Bank, A.C. Gossard, A.J. Taylor, R.D. Averitt, Optics Lett. **32**(12), 1620 (2007)
22. H.T. Chen, W.J. Padilla, J.M.O. Zide, A.C. Gossard, A.J. Taylor, R.D. Averitt, Nature **444**(7119), 597 (2006)
23. H.T. Chen, J.F. O'Hara, A.K. Azad, A.J. Taylor, R.D. Averitt, D.B. Shrekenhamer, W.J. Padilla, Nat. Photon **2**(5), 295 (2008)

3.3 Test and Characterization

3.3.1 Terahertz Time-Domain Spectroscopy (THz-TDS)

The significance of the terahertz, or far-infrared, region of electromagnetic spectrum was shown in Chap. 1, with applications ranging from astronomy to biological sciences. In spite of its significance, terahertz spectroscopy devices were in infancy till the late 1980s primarily due to the difficulty of building devices in that frequency regime. Electronic sources and detectors for millimeter and sub-millimeter waves were limited to about 100 GHz. Fourier Transform Infrared (FTIR) spectroscopy, on the other hand, was useful only above 5 THz due to lack of powerful incoherent sources. The advent of lasers motivated research in far-infrared generation using the difference-frequency generation in non-linear crystals [23], which served as the seed for the development of terahertz time-domain spectroscopy (THz-TDS) [24–28], which still serves as a system of choice for high dynamic range THz spectroscopy. The THz-TDS system generated a great deal of interest in THz imaging after first images acquired using the THz-TDS was reported in 1995 [29].

THz-TDS system is based on single-cycle bursts of electromagnetic transients generated opto-electronically using femtosecond duration laser pulses. Typically, the single-cycle burst are of 1 ps duration whose spectral density spans from near 100 GHz to above 5 THz. Optically gated detection allows direct sampling of the generated terahertz wave with sub-picosecond accuracy. From this measurement, the real and imaginary part of the dielectric function of the medium can be extracted without the use of Kramers-Kronig relation (Eq. (2.11)).

Compared to other THz spectroscopic systems, THz-TDS systems generally offer higher signal-to-noise ratio, a wide spectral band (0.1–5 THz), and faster acquisition time.

3.3.1.1 Terahertz Time-Domain Spectrometer

Figure 3.7 shows the schematic of a terahertz time-domain spectrometer. It consists of a femtosecond laser source, a beam splitter to split the laser beam into two path, one for the photoconductive THz transmitter and the other (through the optical delay line) for the optically gated photoconductive THz receiver. A set of collimating optics is used to focus the THz wave onto the sample and the THz receiver. An optical copper is used in the transmitting laser path which along with the lock-in amplifier serves as coherent mixer to eliminate DC and low-frequency noise in the system. The computer controls the delay line and measures the amplified, lock-in detected photocurrent versus path length. After capturing the entire THz pulse, the desired spectral response is generated using the Fast Fourier Transform (FFT). In the next few paragraphs we will describe the function of each component of the spectrometer.

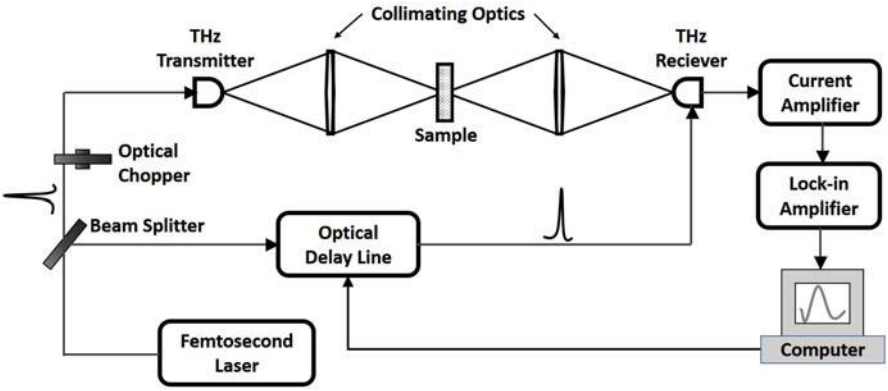

Fig. 3.7 Schematic of a typical THz time-domain spectrometer using a femtosecond laser source and photoconductive THz transmitter and receiver

3.3.1.2 Laser Sources

Solid-state laser sources like the Ti:Sapphire laser [30] with wavelength around 800 nm have largely displaced the older dye lasers [31] and they are a mature and commercial product now. The typical repetition rate of these lasers is about 100 MHz with 10–50 mW of laser power that is sufficient for most of the THz transmitters and receivers. Recent development of all-solid-state femtosecond lasers [32] will result in lasers that are more practical, compact, and cost-effective.

3.3.1.3 THz Transmitters and Detectors

Both the THz transmitter and receiver are based on the photoconductive ("Auston") switch [26, 33], which consists of a semiconductor bridging the gap in a transmission line or a dipole antenna structure as shown in Fig. 3.8a. The response of the voltage biased photoconductive antenna to a pulsed laser source is shown in Fig. 3.8b. The current through the switch rises rapidly at the incidence of the laser pulse and decays at a rate proportional to the carrier lifetime of the bridging semiconductor, generating a picosecond-rate transient current $J(t)$. The transmission line or the dipole antenna is designed such that this transient current is radiated into the free space.

To convert the photoconductive switch to a receiver, a trans-impedance amplifier (current-to-voltage converter) is connected across the switch instead of the voltage bias. The electric field in the bridging gap is now provided by the incident THz pulse. The current only flows through the receiving switch, the photodetector, when carriers are generated by the incident laser source resulting in photoconductive sampling of the THz pulse as shown in Fig. 3.8c. Since electronics are not fast enough to sample the picosecond THz pulse directly, repetitive measurement of the

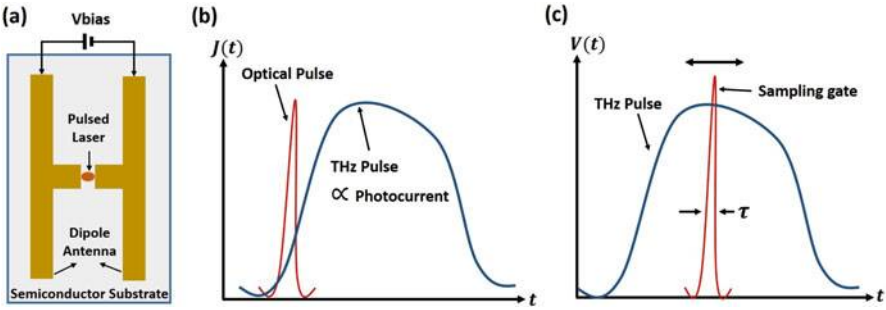

Fig. 3.8 (**a**) Photoconductive "Auston" switch integrated in a THz dipole on a substrate. Laser pulses are focused onto the gap in the dipole antenna which inject carriers into the substrate, which are swept across the dipole due to the bias voltage across. (**b**) Typical current response $J(t)$ of a photoconductive switch to a short laser pulse. (**c**) Photoconductive sampling measures the THz pulse $v(t)$ within the sampling interval τ

photoconductive sample is used for each sample point. If the photo-carrier lifetime, τ, is much shorter than the THz pulse, the photoconductive switch acts as a sampling gate for the THz pulse. Since the laser pulse which triggers the transmitter and gate the detector originate from the same source, the relative delay can be controlled through a optical delay line (Fig. 3.7) and the entire THz pulse is sampled step by step.

Although transmitter and receiver structures are similar in principle, photoconductive switches are designed specifically for transmitters [26, 34, 35] and receivers [26, 36] for better efficiency.

3.3.1.4 Bandwidth Limitation of THz Detectors

The photocurrent transient of the detector $J(t)$ can be expressed as the following convolution:

$$J(t) = \int \sigma(t - t')E(t')dt' \tag{3.6}$$

where $\sigma(t)$ is the transient photoconductivity and $E(t)$ is the incident electric field of the THz pulse. $E(t)$ is faithfully reproduced by $J(t)$ when the photoconductive transient is much shorter than the THz pulse. The high-frequency response of the detector is determined by the photoconductive transient and the low-frequency response is determined by the antenna structure.

The photocurrent decay time needs to be less than 0.5 ps in order to resolve transients in the THz regime. The intrinsic carrier lifetime in semiconductors is far slower, therefore the carrier lifetime needs to be reduced below its intrinsic value, commonly achieved by introducing defect states that have a fast carrier capture rate, either during crystal growth or afterwards through ion implantation.

Low temperature grown GaAs (LT-GaAs) [37] and radiation-damaged silicon-on-sapphire (RD-SOS) [38] are two such examples.

The electric field across the photoconductor can differ from the incident THz field due to the frequency response of the antenna structure.

3.3.1.5 Collimating and Focusing Optics

An important part of both the transmitter and receiver photoconductive antenna is the substrate lens. Because of the presence of the substrate on one side of photoconductive antenna, a substrate lens is required to efficiently couple the THz radiating pulse from the dipole to the free space and also magnifies the dipole antenna, increasing the antennas efficiency as well [39].

In order to incorporate the THz source and detector antennas into a spectroscopy system, a THz optical system required that can guide the THz wave from the source to the detector and focus it on to a diffraction-limited spot at the sample, and such a system is shown in Fig. 3.9. The THz radiation which is coupled into free space using substrate lenses is collimated and focused using a pair of off-axis parabolic mirrors (OAPM). This parallel, diffraction-limited collimated beam can be focused to a diffraction-limited spot at the sample using a pair of focusing lenses or OAPMs (dashed box in Fig. 3.9).

Although the OAPMs are difficult to align, they offer high reflectivity and achromatic operation over the entire THz range and visible lasers can be used for alignment. Fused quartz lenses can be used as an alternative for frequencies below 1 THz and up to 10 THz with silicon lenses but alignment with visible light or laser is not possible. Another useful lens is TPX (poly-4-methyl-pentene-1), a polymer which has low absorption and dispersion throughout the THz range [40], but is difficult to polish for their softness.

Alignment of OAPMs is covered in detail in Sect. 3.3.3.

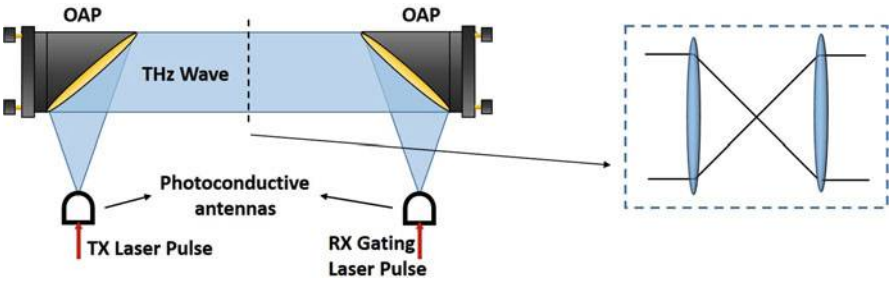

Fig. 3.9 The THz radiation is coupled in and out of the photoconductive antennas using substrate lenses and collimated using a pair off-axis parabolic mirrors (OAPM). Optionally, a pair of lenses or OAPMs can be used to focus the THz wave to a diffraction-limited spot at the sample (*dashed box*)

3.3.1.6 Lock-In Detection

Lock-in detection is primarily used when the desired signal is buried in the noise of the measurement system and cannot be measured directly. The received signal to be measured, $V_{\text{signal}}(t)$, is typically contaminated by offset and noise that can be expressed as [41]

$$V_{\text{signal}}(t) = V_{\text{IN}} + V_{\text{offset}} + V_{\text{white-noise}}(t) + V_{\text{flicker-noise}}(t) \tag{3.7}$$

where V_{IN} is the desired DC signal to be measured, e.g. optically gated THz electric field, V_{offset} is the DC offset voltage present both in the optics and electronics of the THz-TDS system, $V_{\text{white-noise}}$ is the *white gaussian* noise in the system which can be eliminated by simple averaging, and $V_{\text{flicker-noise}}(t)$ is the *flicker noise* which is inversely proportional to frequency $(1/f)$. Even if we can remove the DC offset voltage by some calibration method and eliminate the white-noise by averaging, the measured signal will still be contaminated by the low-frequency drift associated with the flicker-noise. One powerful technique to remove the offset and the drift is by intentionally chopping the signal "on" ($V_{\text{IN-ON}}$) and "off" ($V_{\text{IN-OFF}}$) and taking the difference ($V_{\text{IN-ON}} - V_{\text{IN-OFF}}$). It can be seen from Eq. (3.7) that the offset voltage can be eliminated as well as low-frequency drift that is lower in frequency than the chopping frequency. And if we average the signal after the difference, the white-noise can also be eliminated, leaving us with only the noise contribution at the chopping frequency. Although this method can be implemented using a combination of analog and digital electronics, an elegant and powerful way is to use a lock-in amplifier.

A typical lock-in detection application is shown in Fig. 3.10 in which a laser is used to illuminate a sample and a detector, along with optics, is used to measure the emitted fluorescence. The laser is chopped at a particular frequency so the fluorescence turns "on" and "off" at that frequency. The same chopping frequency is provided as reference to the lock-in amplifier for it to "lock" and determine the operating frequency. Typically, the reference is converted to a sinusoid using a voltage-controlled oscillator (VCO) [42] with an adjustable phase which is multiplied with the input signal and time averaged to form the output voltage V_{out}

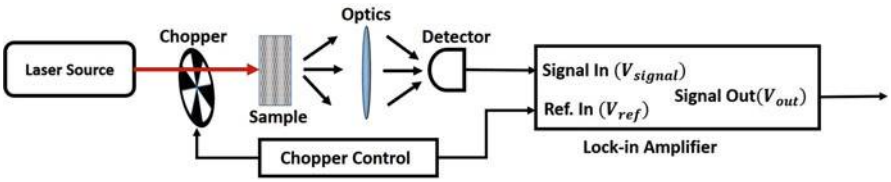

Fig. 3.10 A typical lock-in amplifier application in which one measures the fluorescence from a sample that is illuminated by a chopped laser source [41]

$$V_{\text{out}} = \langle V_{\text{signal}}(t) \cos(\omega t + \phi) \rangle \tag{3.8}$$

This method will pick out the fundamental Fourier component of the signal, $V_{\text{signal}}(t)$, which is proportional to the desired DC value, V_{IN}. This multiplying function is carried out by analog or digital electronics called mixer or a phase sensitive detector (PSD) [42]. Lock-in systems are sometimes referred to as special purpose *correlators* [43]. Most lock-in amplifiers are dual phase systems that incorporate a pair of PSDs which enables them to measure both the *in-phase* and *quadrature* component of the coherent input signal [43], allowing them to measure the magnitude and phase of the input signal.

3.3.1.7 Terahertz Time-Domain Data Analysis

As with most spectroscopic techniques, THz-TDS requires two measurements: one reference waveform $E_{\text{ref}}(t)$ measured without the sample or with sample with known dielectric properties and, the second waveform $E_{\text{sample}}(t)$, in which the radiation interacts with the sample. In order to observe the spectrum of the measurement, $E_{\text{ref}}(t)$ and $E_{\text{sample}}(t)$ can directly be Fourier-transformed to obtain the respective spectra, $E_{\text{ref}}(\omega)$ and $E_{\text{sample}}(\omega)$. One such example, where the absorption properties of methamphetamine (MA) is studied in the frequency range of 0.2–2.6 THz [44], is shown in Fig. 3.11. An useful trick which helps improve the readability of the measurement is a differential spectra that can be expressed as

$$\Delta E(\omega) = \frac{E_{\text{sample}}(\omega) - E_{\text{ref}}(\omega)}{E_{\text{ref}}(\omega)} \tag{3.9}$$

This technique is particularly useful when the difference between the sample and reference is very small.

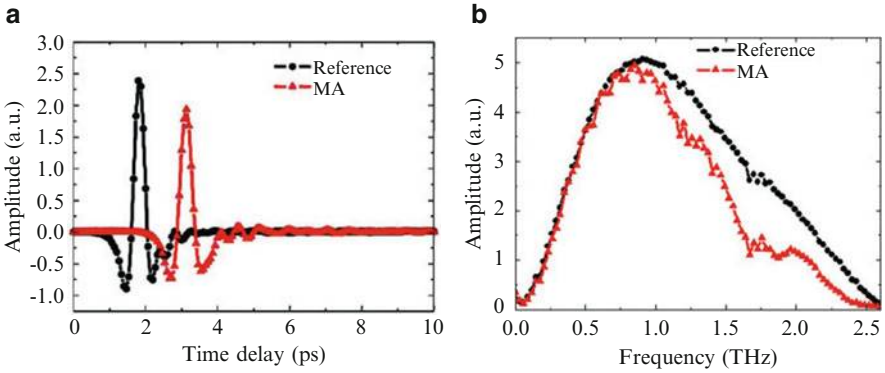

Fig. 3.11 (**a**) THz time-domain transmissive plot of the reference (no sample) and the sample, MA (methamphetamine) and (**b**) corresponding THz frequency-domain spectra [44]

Typically, the time-domain data is modified before performing the Fourier-transform on it, mostly to remove reflections that are prominent when a sample is thick. A thick sample is defined as one for which the transit time of the THz pulse is much larger than its duration. Semiconductor samples typically have their substrate thickness ranging from 100–500 μm, making them a thick medium. Because the measurement is done in time-domain, substrate reflections can be windowed out of the raw data without much loss in spectral resolution or accuracy. The Fresnel coefficients for transmission and reflection are used to remove the artifacts from multiple reflections at the boundary of the sample [39].

3.3.2 *Continuous-Wave (cw) Terahertz Spectroscopy*

Although THz-TDS have their advantages, continuous-wave, or frequency-domain, terahertz spectrometers are becoming popular because of their low-cost and ease of operation. Additionally, they offer the advantage of higher resolution with precise frequency control, compact footprint since a delay stage is not necessary and typically they use diode lasers which remain more cost-efficient than pulsed lasers used in THz-TDS.

3.3.2.1 A Continuous-Wave Terahertz (cw-THz) Spectrometer

Optical heterodyning is becoming a established standard for generating continuous-wave terahertz wave [45], and distributed feedback (DFB) lasers are becoming the standard in optical source because of their compact size, cost-effective, and hassle-free solution. A typical continuous-wave terahertz (cw-THz) spectroscopy setup is shown in Fig. 3.12 as implemented in one of the commercial products, Toptica

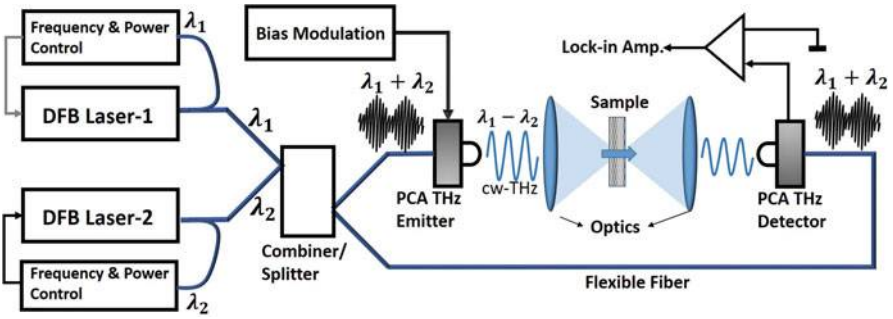

Fig. 3.12 Schematic of a typical continuous-wave terahertz (cw-THz) spectrometer. The continuous terahertz wave is created using the beat frequency of two distributed feedback (DFB) lasers that is transmitted and detected using photoconductive antennas

TeraScan [46]. Using interferometric frequency control [47], two DFB laser diodes are tuned to adjacent wavelengths λ_1 and λ_2 (e.g., 853 nm and 855 nm). The two-lasers are superimposed using a combiner and optionally, the two-color laser can be amplified for higher power. Using a 50:50 fiber splitter, two fiber outputs are created to irradiate the transmit and receive photomixers made from interleaved metal-semiconductor-metal structures. Resonant antenna around the photomixers help in radiating and receiving the terahertz wave of the beat frequency ($\lambda_1 - \lambda_2$). The bias is usually modulated to function as the optical chopper in the lock-in detection as explained in Sect. 3.3.1.

3.3.2.2 Laser Sources

Distributed feedback (DFB) lasers have established themselves as a compact, cost-effective, and carefree alternative to traditional lasers like the Ti:Sapphire laser [30]. DFB lasers at 0.8 μm have become the preferred choice for GaAs photomixers [46–50], because of their high thermal tuning coefficient of ~25 GHz/K per diode [51], resulting in about 2000 GHz scanning frequency. DFB diodes feature a grating structure within the active region of the semiconductor [48] (see Fig. 3.13a), restricting their emission spectrum to a single longitudinal mode. Varying the grating pitch either thermally or electrically tunes the lasing wavelength, and continuous frequency scans of 2000 GHz can be realized by means of a temperature sweep of 50 K. For frequency stabilization as well as controlled frequency tuning, each DFB laser is thermally and electrically regulated by an electronic feedback as shown in Fig. 3.12. The temperature is mostly controlled by a thermo-electric cooler (TEC) [52], and the frequency of the laser is measured using a fiber-coupled quadrature interferometer [47] (see Fig. 3.13b). Alternatively, instead of using a feedback scheme, the thermo-electric control is calibrated and values stored in a look-up table that can be used to control the DFB laser, based on frequency sensed from the quadrature interferometer [52].

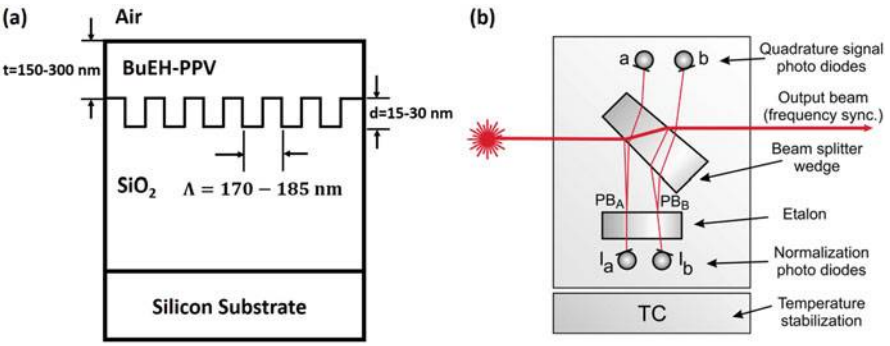

Fig. 3.13 (**a**) Schematic of a polymer DFB laser (not drawn to scale) [48]. (**b**) Quadrature interferometer for frequency control of DFB lasers [47]

3.3.2.3 THz Transmitters and Detectors

Typically, a transmitting photomixer consists of an epitaxial layer of low-temperature-grown gallium arsenide (LTG-GaAs) with interdigitated electrodes fabricated on a semi-insulating GaAs substrate. Two-lasers illuminating the gaps between the electrodes generate difference frequency photocurrents, and terahertz power is generated as the photocurrents drive the integrated antenna. The advantages of LTG-GaAs are its short photoconductive lifetime ($\tau < 1\,\text{ps}$) and its high electrical breakdown ($E_B > 5 \times 10^5\,\text{V} \cdot \text{cm}^{-1}$) [45]. New generation of terahertz sources and detectors are made up of high-energy ion-implanted GaAs interdigitated photomixers [46], which offer the advantage of highly reproducible photoconductive materials. The photomixers are integrated within self-complementary log-periodic spiral [46] or linear spiral [45] broadband antennas to achieve nearly constant antenna impedance in the frequency range above about 100 GHz [53]. Alternatively, bow-tie antennas are used for polarized input and output [52]. In order to suppress back-reflections and for pre-collimation, the terahertz radiation is coupled to free space via a hyper-hemispherical silicon lens. Scanning electron micrograph of a photomixer with integrated spiral antenna [45] is shown in Fig. 3.14a and the SEM picture of an interdigitated electrodes with integrated bow-tie antenna is shown in Fig. 3.14b [52]. Receiver photomixer and the integrated antennas are usually adapted to the transmitter antennas for better sensitivity. The incident THz field is sampled coherently using the same two-color laser as used for the transmitter.

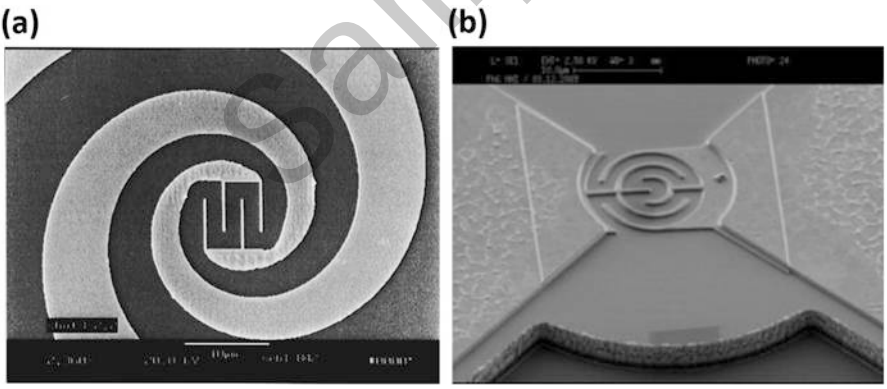

Fig. 3.14 (**a**) Scanning electron micrograph (SEM) picture of electrode region and first turn of spiral antenna for 8 μm × 8 μm photomixer [45]. (**b**) SEM picture of the interdigitated electrodes on the pc material with integrated bow-tie antenna, used in a cw terahertz receiver modules [52]

3.3.2.4 Data Analysis

The detected DC photocurrent (typically $\sim$ *pA*) is preamplified using a transimpedance amplifier and measured using lock-in technique. The principle of lock-in technique is as described in Sect. 3.3.1. Instead of mechanical chopping, typically, the bias voltage of the transmit photomixer is modulated ($\sim \pm 10$ V and up to 10 kHz), which offers the advantage of less noise and no mechanical parts [47]. The photocurrent I_{ph} is proportional to the incident THz electric field, E_{THz}, and the phase difference $\Delta\phi$ between the THz field and the laser beat frequency [46]

$$I_{\text{ph}} \propto E_{\text{THz}} \cos(\Delta\phi) = E_{\text{THz}} \cos(2\pi \Delta L \nu / c) \tag{3.10}$$

where ν is the terahertz frequency, c is the speed of light, and

$$\Delta L = (L_S + L_{\text{THz}}) - L_D \tag{3.11}$$

is the difference between the optical path L_D traveled by the laser beat to the detector and the optical path L_S of the laser beat to the terahertz source plus the terahertz path L_{THz} from the source to the detector.

One possible way to separate the amplitude and phase of the terahertz signal for any given frequency is to vary L_{THz} and thus ΔL with the help of a variable delay stage [47, 53]. Alternatively, the phase difference $\Delta\phi$ can be varied by scanning the terahertz frequency ν, which has the advantages of avoiding any mechanically moving parts and of a much higher scanning rate (up to 10 Hz, depending on the selected lock-in time). In this case, the detected photocurrent I_{ph} oscillates as a function of frequency (see Fig. 3.15a), and the oscillation period is set by the

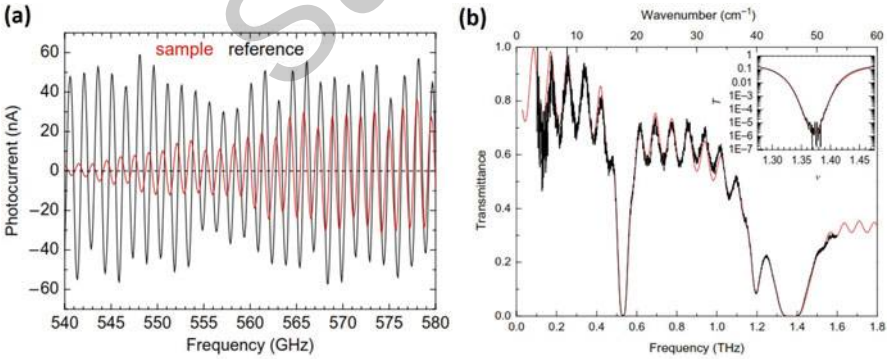

Fig. 3.15 Example of detected terahertz photocurrent and its transmittance plot [46]. (**a**) Photocurrent with and without a sample (α-lactose monohydrate). The period of interference pattern $\Delta\nu \approx 1.5$ GHz with a optical path difference $\Delta L \approx 0.2$ m (see Eq. (3.11)). (**b**) Transmittance $T(\omega)$ of α-lactose monohydrate for a thickness of $d \approx 1$ mm. The *red line* depicts a fit according to the DrudeLorentz model. Inset: $T(\omega)$ around the absorption feature at 1.369 THz, plotted on a log scale

choice of ΔL. Both the amplitude and phase can be derived from it. The resultant spectra is extracted by calculating the envelope of the oscillating photocurrent (see Fig. 3.15b). Using the extremas, the effective frequency resolution for amplitude can be expressed as $c/(2 \times \Delta L)$ and since phase information can be extracted between an extrema and its adjacent zero-crossing, the frequency resolution for phase can be expressed as $c/(4 \times \Delta L)$ [46]. Thus the spectral resolution of the phase can be adapted easily by varying the optical path difference ΔL (see Eq. (3.11)).

The transmittance of a sample $T(\omega)$ can be determined by comparing the envelopes of the sample and reference spectra,

$$T(\omega) = \frac{I_{\mathrm{ph}}^{\mathrm{sample}}(\omega)}{I_{\mathrm{ph}}^{\mathrm{ref}}(\omega)} \tag{3.12}$$

where $I_{\mathrm{ph}}^{\mathrm{ref}}(\omega)$ and $I_{\mathrm{ph}}^{\mathrm{sample}}(\omega)$ are the spectra of the reference and the sample, respectively. For cases where the difference between the sample and reference is small, a useful trick to improve the readability of the data is to plot the differential spectra,

$$\Delta T(\omega) = \frac{I_{\mathrm{ph}}^{\mathrm{sample}}(\omega) - I_{\mathrm{ph}}^{\mathrm{ref}}(\omega)}{I_{\mathrm{ph}}^{\mathrm{ref}}(\omega)} \tag{3.13}$$

An example of the detected terahertz photocurrent with and without a sample (α-lactose monohydrate) and its transmittance $T(\omega)$ is shown in Fig. 3.15 [46].

3.3.3 *Optical Alignment of Off-Axis Parabolic Mirrors*

For every THz spectroscopy system, a set of optics is needed to guide the THz wave from the source to the detector, through the sample if necessary, to make transmissive or reflective measurements (see Sect. 3.3.1.5). An optical system involving reflective surfaces (spherical, paraboloidal, etc.) offers many advantages over refractive systems (Teflon lenses, TPX (poly-4-methyl-pentene-1) lenses, etc). All-reflective optical systems have wide bandwidth and no chromatic aberration, allowing it to be tested and aligned at one frequency (e.g., visible) and spectroscopy at another (e.g., THz) without worrying about realignment.

The parabola is one of the most preferred aspheric surface geometries used for collimating-focusing optical setups. When a collimating beam is incident parallel to the optical axis of the parabola (see Fig. 3.16), the beam is focused to a point image at the focal point of the parabola. Conversely, a point source at the same focal point generates a collimating beam.

In most spectroscopy setups, including THz spectroscopy, the focal point must be placed out of the incident collimated beam [22, 54–56]. For this purpose, the

Appendix A
Electromagnetic Waves

A.1 Helmholtz's Equation

Taking the curl of $\nabla \times \mathbf{E} + \frac{\partial \mathbf{B}}{\partial t} = 0$ in Eq. (2.4):

$$\begin{aligned} \nabla \times (\nabla \times \mathbf{E}) &= -\nabla \times \left(\frac{\partial \mathbf{B}}{\partial t}\right) \\ \nabla(\nabla \cdot \mathbf{E}) - \nabla^2 \mathbf{E} &= -\mu\epsilon \frac{\partial^2 \mathbf{E}}{\partial t} \\ \nabla^2 \mathbf{E} + \mu\epsilon \frac{\partial^2 \mathbf{E}}{\partial t} &= 0 \end{aligned} \tag{A.1}$$

Similarly, the other part of the Helmholtz's equation can be solved by taking curl of $\nabla \times \mathbf{H} - \frac{\partial \mathbf{D}}{\partial t} = 0$ in Eq. (2.4).

A.2 Electromagnetic Waves *Are* Transverse

Let us consider a plane wave (in x-direction) that satisfies both Maxwell's and Helmholtz's equation

$$\begin{aligned} \mathbf{E}(\mathbf{x}, t) &= \mathbf{E}_0 e^{i(kx - \omega t)} \\ \mathbf{B}(\mathbf{x}, t) &= \mathbf{B}_0 e^{i(kx - \omega t)} \end{aligned} \tag{A.2}$$

S. Rout, S. Sonkusale, *Active Metamaterials*, DOI 10.1007/978-3-319-52219-7

Whereas every solution to Maxwell's equations (in empty space or nonconductors) must obey the wave equation, the converse is *not* true; it imposes special constraints on $\mathbf{E}_0$ and $\mathbf{B}_0$. Let us consider $\mathbf{E}(\mathbf{x}, t)$ with three orthogonal components as

$$\mathbf{E}(\mathbf{x}, t) = \left(\mathbf{E}_{0x} + \mathbf{E}_{0y} + \mathbf{E}_{0z}\right) e^{i(kx-\omega t)} \tag{A.3}$$

Since $\nabla \cdot \mathbf{E} = 0$,

$$\frac{\partial \mathbf{E}_{0x} e^{ikx}}{\partial x} + \frac{\partial \mathbf{E}_{0y} e^{ikx}}{\partial y} + \frac{\partial \mathbf{E}_{0z} e^{ikx}}{\partial z} = 0 \tag{A.4}$$

Equation (A.4) is satisfied only if

$$\mathbf{E}_{0x} = 0 \tag{A.5}$$

Similarly, it can be shown that

$$\mathbf{B}_{0x} = 0 \tag{A.6}$$

Moreover, it can be shown from Faraday's law, $\nabla \times \mathbf{E} = -\partial \mathbf{B}/\partial t$ that

$$\mathbf{B}_0 = \frac{k}{\omega}\left(\hat{i} \times \mathbf{E}_0\right) \tag{A.7}$$

Thus, Eqs. (A.5)–(A.7) show that the EM plane wave needs to be *transverse* with the vectors $\mathbf{B}_0, \mathbf{E}_0, k$ forming a right-handed triplet.